

Poly(9-vinyl carbazole)/Fullerene Heterointerface for Organic Solar Cells and Photovoltaics Applications – First-Principles Study

Edwin Okoampa Boadu ¹, Van Wellington Elloh ^{1,2,*}, Abu Yaya ³

¹ Department of Biomedical Engineering, Koforidua Technical University, Koforidua, Ghana; okoampa.boadu@ktu.edu.gh (E.O.B.);

² Department of Physics, School of Engineering, University of Petroleum and Energy Studies (UPES), Dehradun, India

³ Department of Materials Science and Engineering, University of Ghana, Legon, Ghana; ayaya@ug.edu.gh (A.Y.);

* Correspondence: vanw.elloh@ktu.edu.gh (V.W.E.);

Scopus Author ID 7801666609

Received: 11.03.2023; Accepted: 28.05.2023; Published: 19.02.2024

Abstract: Photovoltaic and solar cell application is a pliable upcoming answer in a sustainable manner to the current energy and environmental menace. The surest and safest means to obtain energy for sustainable development is by employing organic polymer photovoltaics. Polymer solar cells are sources of inexpensive and renewable energy. They are excellent sources of low-cost energy production. Tailoring carbon nano polymeric materials' optical, electronic, and chemical properties to suit various applications by appropriate modification sets has gained significant interest. Highly ordered aggregation of conjugated oligomers and polymers can improve properties such as charge transfer and interaction with light processes, leading to better device performance. Structural and morphological characterization of organic materials in the solid state is relevant for their application in organic photovoltaics. The current manuscript showcases the construction of a novel hybrid carbon nanomaterial with fascinating electronic and chemical properties and tunable energy band gap of a nano heterojunction comprising "poly(9-vinyl carbazole), PVK and fullerene, C₆₀. A comprehensive investigation of PVK/C₆₀ adsorption surface is investigated using ab-initio density functional theory calculations with van der Waals corrections (GGA+vdW) implementation. The band gap values we have calculated in this work are low enough to make the nanoheterostructure exceedingly promising for photovoltaic applications.

Keywords: heterointerface; density functional theory; optoelectronics; heterointerface; solar cells; photovoltaics.

© 2024 by the authors. This article is an open-access article distributed under the terms and conditions of the Creative Commons Attribution (CC BY) license (<https://creativecommons.org/licenses/by/4.0/>).

1. Introduction

Since the invention of the first silicon solar cell [1], solar cells have demonstrated great potential in utilizing renewable solar energy. After decades of development, the solar cell family is currently composed of Si cells, inorganic thin film technologies, and emerging photovoltaics (PV). Si and various inorganic thin film solar cells have been successfully commercialized, while at the same time, the performance of emerging PV, containing OSCs, dye-sensitized solar cells (DSSCs), perovskite solar cells (PSCs), and so on, also gained

considerable improvement. Compared with other PV technologies, OSCs have drawn broad interest owing to their advantages, such as being low-cost, flexible, semitransparent, non-toxic, and ideal for roll-to-roll large-scale processing. According to research, the PCE of OSCs has shown a rapid increase in the past few years, with the state-of-the-art OSCs yielding a certified PCE of 18.2% [2], which shows their potential for future practical applications.

The first generation of OSCs was born with a single active layer sandwiched between two electrodes with different work functions. However, the single-layer devices showed poor PCE below 0.1% for the reason of difficulty in achieving efficient dissociation of excitons (electron-hole pairs) and severe recombination of electrons and holes [3]. A bilayer heterojunction structure containing copper phthalocyanine as donor (D) and perylene tetracarboxylic derivate as acceptor (A) was introduced by Tang [4], which was regarded as a big forward step in the field of OSCs. Nevertheless, the limited D/A interface area still worked against the efficient exciton diffusion and separation, thus not yielding a high PCE in bilayer OSCs [5]. Yu *et al.* [6] proposed the bulk heterojunction (BHJ) OSCs, in which the donor and acceptor were mixed together to serve as the active layer. The BHJ structure presented an enhanced D/A interface and reduced the diffusion distance for exciton separation, significantly improving device performance. Since the invention of the BHJ structure, which was considered a breakthrough in OSCs, the PCE of BHJ OSCs has skyrocketed to over 18% [7–10], making it a promising PV technology.

The field of OSCs has advanced enormously in the last few decades, with frequent reports of lab-scale efficiencies of over 20% [11–28]. A large part of this progress can be attributed to the development of new light-absorbing materials. Starting from the simple homopolymers as donors and fullerene derivatives as acceptors that were popular in the early days of the field, hundreds of more complex materials for donor and acceptor have been introduced with improved optoelectronic characteristics, containing light absorption, charge generation, and charge transport. Significant advances have also been made in other integral components of OSCs, including electrodes and interlayers. In addition, novel device structures such as ternary and tandem OSCs have also gained increasing attention with the great progress achieved in light-absorbing materials.

In BHJ OSCs, conversion of incident photons into electric current involves four fundamental steps viz, light absorption and exciton generation, exciton diffusion to D/A interfaces, exciton dissociation at D/A interfaces to form a germinate pair, and the charge separation and transport, which is then collected by the respective electrodes under an internal electric field [30–35]. When the active layer of BHJ OSC absorbs the photons, the excitation can occur via two kinds of paths. Firstly, the excitation forms in the donor, which is then followed by the electron transfer from donor to acceptor. Secondly, the excitation forms in the acceptor, which is then followed by the electron transfer from the acceptor to the donor. Generally, owing to the different absorption abilities of acceptors, step one dominates the photocurrent generation in fullerene-based OSCs, while in non-fullerene OSCs, steps one and two contribute to the generation of photocurrent.

As a potential sustainable energy technology, organic photovoltaics (OPVs) have attracted significant attention from both academia and industry [36, 37]. OPVs have been developed for over three decades. Their power conversion efficiency (PCE) has recently improved from less than 1% to approximately 19% [38–42]. The key driving force for the increase in PCE is the development of photoactive materials. In particular, in recent years, the rapid development of narrow bandgap small-molecule acceptors has substantially improved

the efficiency of OPV [43-46]. The complex chemical structure of small-molecule acceptors compared with that of fullerene-based acceptors causes the bulk heterojunction (BHJ) active layer to display stronger absorption in the near-infrared and tunable energy levels [47-54]. These cause OPV to have higher photocurrent and open-circuit voltage. Narrow bandgap small-molecule acceptors have strongly improved the properties of OPV because of their high efficiency, stability, indoor performance, and semitransparency toward commercial applications owing to their effective molecular designs [55-62].

The most attractive advantages of OPVs are their solution-processability and remarkable mechanical flexibility [63-69]. These can be compatible with large-scale production, such as roll-to-roll printing, reducing production costs and realizing commercial applications [70-77]. Solution-processed and flexible OPVs based on fullerenes have been widely reported [78-88]. However, the efficiency of solution-processed flexible OPVs is limited by fullerene system materials and remains at a low level. The development of narrow bandgap small-molecule acceptors can overcome the bottleneck of solution-processed flexible OPVs [89]. The introduction of high-efficiency active layers causes a substantial increase in the efficiency of solution-processed flexible OPVs [90]. The active layer of OPVs is generally composed of a blend of donor and acceptor materials. In recent decades, blends with polymers as donors and fullerenes as acceptors have been studied extensively [91]. In this work, myriads of PVK/C60 structural permutations have been constructed and examined. Based on different orientations and stacking patterns, optical spectral absorption, transfer of charge, and chemical processes were explored utilizing DFT methods by incorporating the van der Waals correction term (GGA+vdW).

2. Materials and Methods

Using the QUANTUM ESPRESSO code version 7.0 [92, 93], we performed our calculations in the density functional theory framework. We adopted for PVK/C60 nanoheterojunction a supercell model. Our supercell was aligned along the z-axis. We set a 15 Å thick vacuum layer in x- and y-directions to avoid interactions between the supercell and its periodic images.

The PVK/C60 nano heterojunction was simulated using periodic boundary conditions. Our calculations were in both LDA, Perdew-Zunger parametrization [94], and GGA, Perdew-Burke-Ernzerhof parametrization [95]. Ultrasoft pseudopotentials [96] were employed to describe interactions between ions and electrons. Description of the exchange-correlation effects were in plane wave basis sets methods. Van der Waals (vdW) interaction was catered for in terms of Grimme's D3 correction term [97]. vdW interactions are well aware of as being significant in systems comprising carbon nanomaterials [98-100].

The kinetic energy cutoff for plane waves was put at 30 Ry, and the charge density cutoff was 180 Ry in the computations. The energy convergence criterion was 0.002 Ry; each atom has a residual force on it less than 0.001 Ryd/Bohr in the relaxation process. A Γ -centered 5x5x1 Monkhorst-Pack scheme [101] was employed. For geometry optimization, we made use of k-point grids for sampling the Brillouin zone. Non-self-consistent field calculation was carried out with a 9x9x1 grid in the computation to determine quantized energy levels. Band structure calculations were along the Γ -Z-direction. VESTA software [102] was utilized to generate the optimized figures. With the aid of xcrystden version 1.5.60 software, [103] we were able to visualize the models.

3. Results and Discussion

3.1. Nano heterostructures.

Figure 1 is an illustration of PVK and C₆₀ nanostructures used for the study.

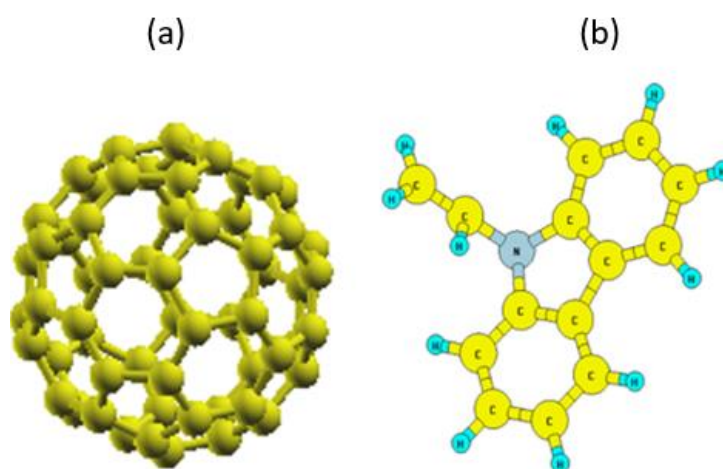


Figure 1. Illustration of PVK and C₆₀ nanostructures.

In this work, we studied three configurations of PVK and C₆₀ nanostructures: in the first case, the five-membered ring of C₆₀ was aligned with the π -conjugate plane of PVK; in the second instance, the six-membered ring of the C₆₀ was positioned side by side with the π -conjugate plane of PVK, and in the third configuration, the six-membered ring of the C₆₀ was arranged axially with the nitrogen-containing ring of the PVK polymer chain.

The stability of the novel PVK/C₆₀ nano heterojunctions was determined by computing adsorption energies and formation energies per atom. Equations (1) and (2) were employed to determine the most energetically favorable stacking nanoheterostructure [104]. 3.383 Å separation distance was ensured to exist between PVK and C₆₀ molecules for all the three nano heterojunctions designed. We calculated interlayer distance which is comparable to graphite interlayer separations (ca. 3.35 Å). The adsorption energies, E_{ad} , were computed for the various PVK/C₆₀ nano heterojunctions and tabulated in Table 1. In this work, we calculated the adsorption energies as shown below:

$$E_{ad} = (E_{PVK/C_{60}} - E_{PVK} - E_{C_{60}}) \quad (1)$$

here, $E_{PVK/C_{60}}$, E_{PVK} , $E_{C_{60}}$ is grand base energy for the composite structure, grand enthalpy for the polymeric structure, and grand energy for C₆₀, respectively, adopting DFT methods.

Table 1. Adsorption energy determined from Relation 1.

GGA+vdW	Adsorption Energy (eV)
PVK/C ₆₀ (1)	1.239
PVK/C ₆₀ (2)	1.418
PVK/C ₆₀ (3)	2.236
LDA	
PVK/C ₆₀ (1)	1.223
PVK/C ₆₀ (2)	1.335
PVK/C ₆₀ (3)	2.129

Whenever $E_{ad} > 0$, it means that adsorption onto the surface is feasible thermodynamically. As E_{ad} value increases, the tendency for the adsorbate molecule to bind onto the PVK/C60 nanoheterostructure surface increases. Table 1 shows the distinctive trends in the preferences for PVK/C60(1), PVK/C60(2), and PVK/C60(3) nano heterojunctions to adsorb favorably onto PVK/C60 surface. From the table, the interactions between PVK and C60 for PVK/C60(1) and PVK/C60(2) nano heterojunctions are considerably weak as compared to PVK/C60(3). Comparing the adsorption value of PVK/C60(3) in Table 1 with the two other configurations, the adsorption energies of PVK/C60(1) and PVK/C60(2) nano heterojunctions are the weakest, i.e., $E_{ad} \sim 1.239, 1.418$ eV, for GGA+vdW exchange-correlation functional and $E_{ad} \sim 1.223, 1.335$ eV for LDA exchange-correlation functional. These processes can be considered as physisorption processes on the surfaces. For PVK/C60(3) nano heterojunction, the adsorption energies, $E_{ad} \sim 2.236$ and 2.129 eV for the respective exchange-correlation functionals are attributed to the orientation and proximity of the nitride functional group of the polymer to the conjugated π -electrons of the fullerene (C60) to chemisorb at the PVK/C60 surface. For the PVK/C60(3) nano heterojunction, the strongest tendency to chemisorb onto the PVK/C60 surface is found, i.e., $E_{ad} \sim 2.236$ eV is due to the strong π - π interactions between the carbazole unit and the fullerene (C60). In Table 2, we tabulated the formation energy values computed using equation (2) below.

$$\Delta E = E_{CHN} - N_C E_C - N_H E_H - N_N E_N \quad (2)$$

where, E_{CHN} is grand energy for ground state of nanoheterojunction. E_C is grand energy for carbon ground state, N_C is number of carbon atoms. E_H , grand energy for the ground state of H, N_H , number of hydrogen atoms, E_N , grand energy for the ground state of N and N_N , number of nitrogen atoms in the nanoheterojunction. Table 2 shows the formation energy per atom computed for each of the nano heterojunctions. Here, all the modeled nano heterojunctions have negative energies of formation for each atom. The constructed novel structures are, therefore, thermodynamically stable. For clearer perspectives of these novel structures, formation energies per atom for C60 and PVK were respectively determined in turn to be -5.2630 eV, -6.4860 eV. They have greater energies of formation per atom values than those in Table 2. The interpretation is that the novel nano heterojunctions are energetically stable and thermodynamically favorable in comparison with the original structures.

Table 2. Formation energies per atom computed from Relation 2.

GGA+vdW	Formation Energy (eV)
PVK/C ₆₀ (1)	-6.183
PVK/C ₆₀ (2)	-8.224
PVK/C ₆₀ (3)	-10.681
LDA	
PVK/C ₆₀ (1)	-5.991
PVK/C ₆₀ (2)	-7.295
PVK/C ₆₀ (3)	-10.169

Per the calculations, PVK/C₆₀(3) is the most favored and the most stable in both GGA+vdW and LDA parameterizations as compared with PVK/C₆₀(1) and PVK/C₆₀(2) nano heterojunctions. Table 3 shows the trend in sizes for PVK/C₆₀(1), PVK/C₆₀(2) and PVK/C₆₀(3) configurations. Energy differences, E_0 (eV), are also depicted for the simulated nano heterojunctions. They show progressive stability from stable to the most stable nano heterojunction.

Table 3. Optimized lattice parameters: a(Å), b(Å), c(Å); energy gap, E_g (eV); energy difference, E_0 (eV) for PVK/C₆₀(1), PVK/C₆₀(2) and PVK/C₆₀(3) nanoheterojunctions.

GGA+vdW	a (Å)	b (Å)	c (Å)	E_g (eV)	E_0 (eV)
PVK/C ₆₀ (1)	9.3283	9.3496	9.4579	1.223	17.362
PVK/C ₆₀ (2)	9.2770	8.5050	9.2936	1.217	9.212
PVK/C ₆₀ (3)	9.1311	10.1133	9.0673	1.121	0.000
LDA					
PVK/C ₆₀ (1)	9.3019	8.6619	8.6958	1.218	15.379
PVK/C ₆₀ (2)	8.8500	7.0067	8.8528	1.201	7.804
PVK/C ₆₀ (3)	9.1350	10.3534	9.1376	1.112	0.000

In all the three nano heterojunctions designed, observation reveals that the bond lengths in C–C are shorter in PVK/C₆₀(1), PVK/C₆₀(2), and PVK/C₆₀(3) designs with 1.3928 Å, 1.3943 Å, and 1.3934 Å respectively in the GGA+vdW model type as compared with the experimental value of 1.42 Å. The C–N bond length for PVK/C₆₀(3) in the LDA model type is 1.3918 Å as compared with 1.4126 Å & 1.4324 Å for PVK/C₆₀(1) and PVK/C₆₀(2), respectively, Table 4.

Table 4. Optimized C–N, C–C & C–H Bond Lengths(Å) of PVK/C₆₀ nano heterostructure.

GGA+vdW	Bond Length (Å)		
	C–N	C–C	C–H
PVK/C ₆₀ (1)	1.4064	1.3928	1.0848
PVK/C ₆₀ (2)	1.4082	1.3943	1.0858
PVK/C ₆₀ (3)	1.4031	1.3934	1.0863
LDA			
PVK/C ₆₀ (1)	1.4126	1.4198	1.0711
PVK/C ₆₀ (2)	1.4324	1.4211	1.0910
PVK/C ₆₀ (3)	1.3918	1.4169	1.0881

Intra-chain interactions are found to be strong in these nano heterojunctions. Shorter bond lengths, consequently, go with strong bonds, and for that matter, the corresponding stable nature of these nano heterojunctions is anticipated. Consequently, C–N bonds became rigid in PVK/C₆₀(3). Shorter C–C bonds in PVK/C₆₀(1) and PVK/C₆₀(2) nano heterojunctions accounted for their stability and rigid nature. These alterations in bond lengths are dictated by the adsorption energies, which are being influenced by the 3.383Å adsorption distance measured. C–C & C–N shorter bond lengths for PVK/C₆₀(1), PVK/C₆₀(2), and PVK/C₆₀(3) designs indicate that their bond strengths have been increased compared with that prior to adsorption. So, they acquire higher binding energies, giving rise to rigid bonds for these designs. Formation energies per atom values differ, as seen in Table 2. This trend depends on the choice of exchange-correlation functionals. LDA outputs are slightly lower than GGA values. The same pattern is portrayed in optimized lattice parameter quantities in Table 3. LDA gives almost diminishing quantities for lattice parameters. GGA+vdW calculations give the bandgap values for PVK/C₆₀(1), PVK/C₆₀(2), and PVK/C₆₀(3) nano heterojunctions as 1.223, 1.217 and 1.121 eV, respectively, while LDA band gap values were calculated to be 1.218, 1.201 and 1.112 eV respectively.

3.2. Electronic properties.

We plotted the nature of the electronic bands for PVK/C₆₀(1), PVK/C₆₀(2) and PVK/C₆₀(3) nano heterojunctions in Figure 2. The mixed hybridization of valence states for N & H with C atoms is the origin of the displayed patterns. Optimized lattice parameters together

with some other essential structural values, are shown in Table 3. Observations from Figures 2(a, b & c) reveal that the nano heterojunctions have narrow and direct band gaps. Both valance and conduction bands are located at the Γ -points. They are promising for photophysical applications. Fabrication of optoelectronic devices thrives well on such materials. Band gaps of our fabricated novel materials are tunable and have essential applications for photovoltaics and solar cells. They will enhance progress in the engineering of band gaps for infrared optoelectronics and nanoelectronics.

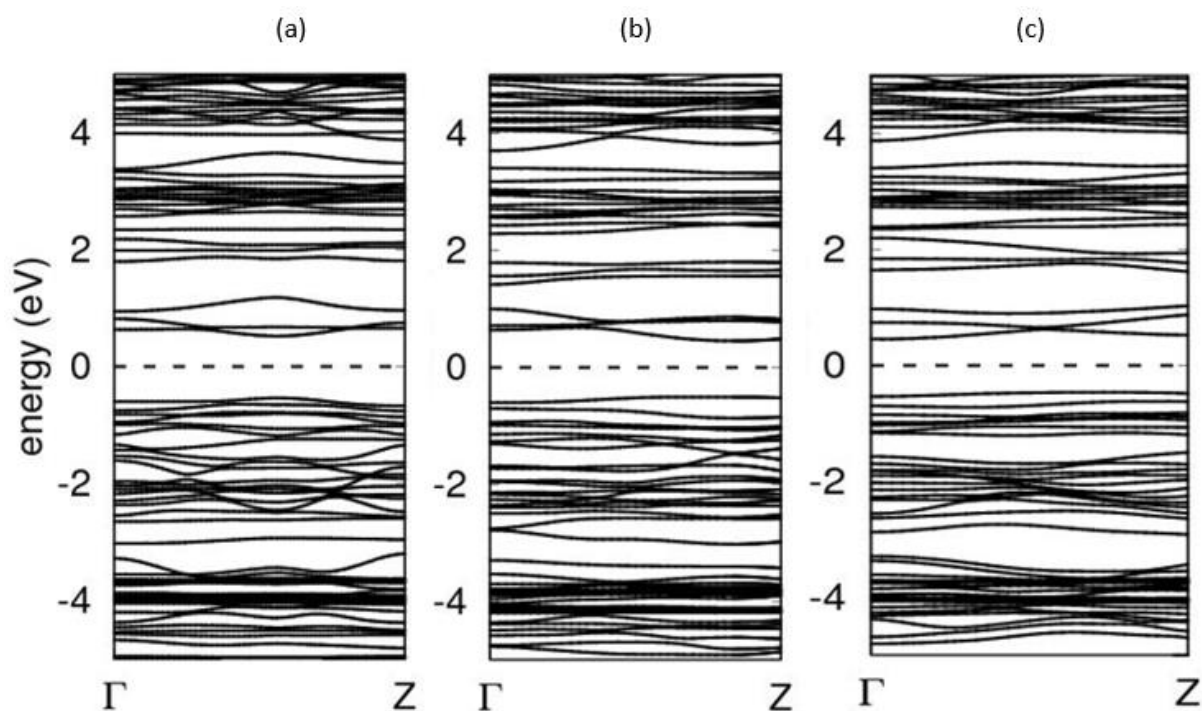


Figure 2. High-symmetry k-points band diagrams for PVK/C₆₀ nano heterojunctions. Zero is designated as Fermi energy for all nano heterojunctions.

3.3 Density of states.

The projected electronic DOS, total DOS, and partial DOS were plotted for the three PVK/C₆₀ nano heterojunctions, as shown respectively in Figures 3, 4, and 5. Using these plots, we made an analysis of interactions arising from the energy gap characteristics of the nano heterojunctions. Fermi energy was designated zero for comparison's sake—the same approach for DOS, which we depicted in Figures 3, 4, and 5. As can be inferred from the plots for DOS, contributors to the valence band are N atoms. Only positive contributions are shown in Figures 3 and 4 for the total and partial density of states for the PVK/C₆₀ nano heterojunctions.

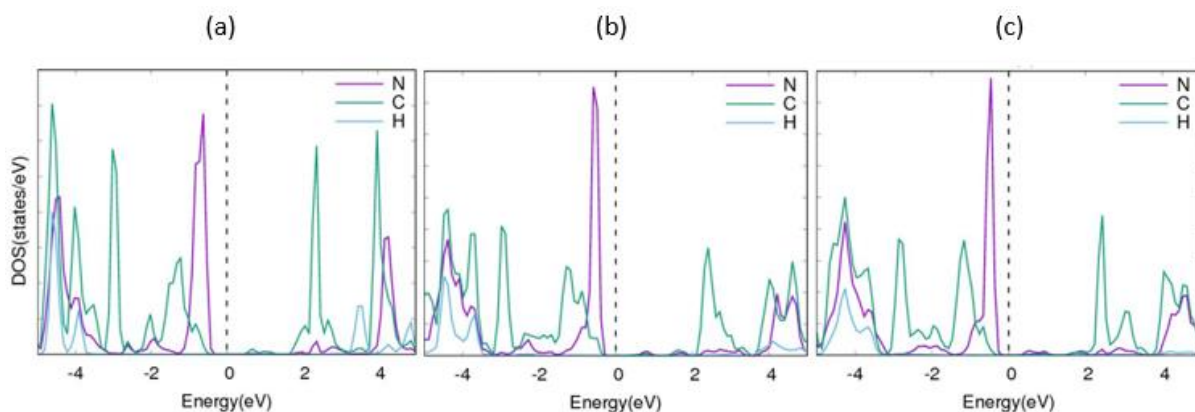


Figure 3. PVK/C₆₀ configuration DOS, setting zero energy for fermi level in nano heterojunctions.

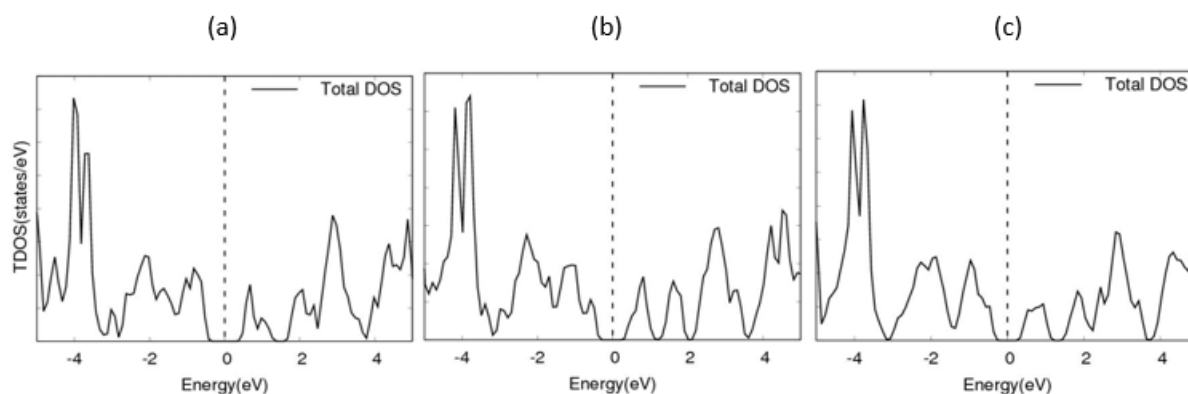


Figure 4. PVK/C₆₀ configuration t-DOS, setting zero energy for fermi level in nano heterojunctions.

Observations from the orbitals picture of atoms reveal DOS close to energy gaps are of p_z character. Atomic N hybridized with p_z states of carbon atoms. From Figure 5, s- and p-orbitals of carbon and p-orbitals of nitrogen dominate the valence and conduction bands. This results in PVK/C₆₀ nano heterojunctions having non-covalent π -stacking characteristics, as depicted by Figures 1(a, b & c).

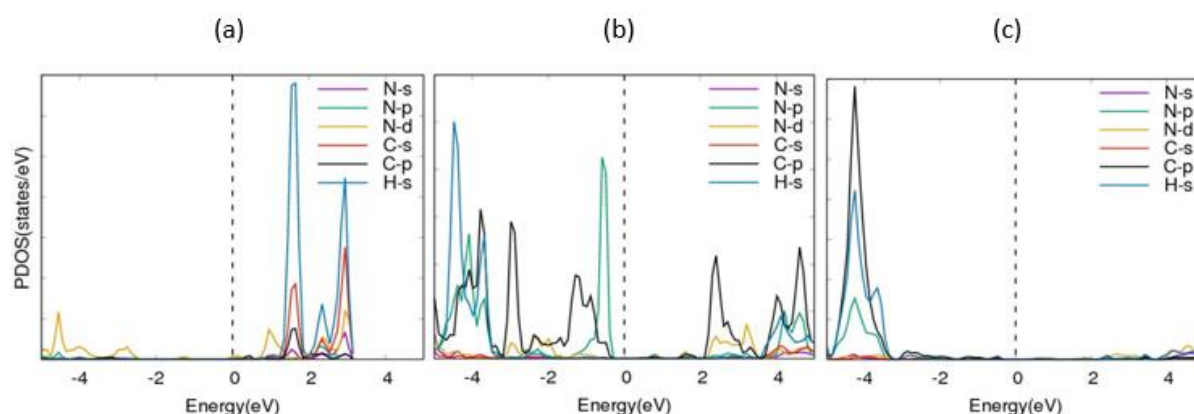


Figure 5. PVK/C₆₀ configuration p-DOS, setting zero energy for fermi level in nano heterojunctions.

3.5 Optical activities.

3.5.1 Spectral absorption.

Optical absorption spectral trend for (a) PVK, (b) C₆₀, (c) PVK/C₆₀(1), (d) PVK/C₆₀(2), and (e) PVK/C₆₀(3) nanostructures are shown in Figures 6(a – e) respectively. Pristine absorption spectra for PVK and C₆₀ are shown in Figures 6(a, b). Spectral absorption calculated for the nano heterojunctions with C₆₀ added is depicted in Figures 6(c – e). Five intensity peaks are located at 0.41, 0.45, 0.49, 0.51, and 0.53 Ry in Figure 6(a). 0.41 Ry is the most intense peak. For each direction, there are distinctive absorption levels, as illustrated by Figure 6(b). Absorption in the Y-direction exceeds absorption in the Z-direction when C₆₀, as indicated in Figures 6(b, c). X-direction has the least absorption. Absorption in the Y- direction exceeds absorption in the Z- direction, Figure 6(e). Absorptions in X-, Y- and Z- directions are nearly similar. Y- Y-direction absorption dominates, Figure 6(b).

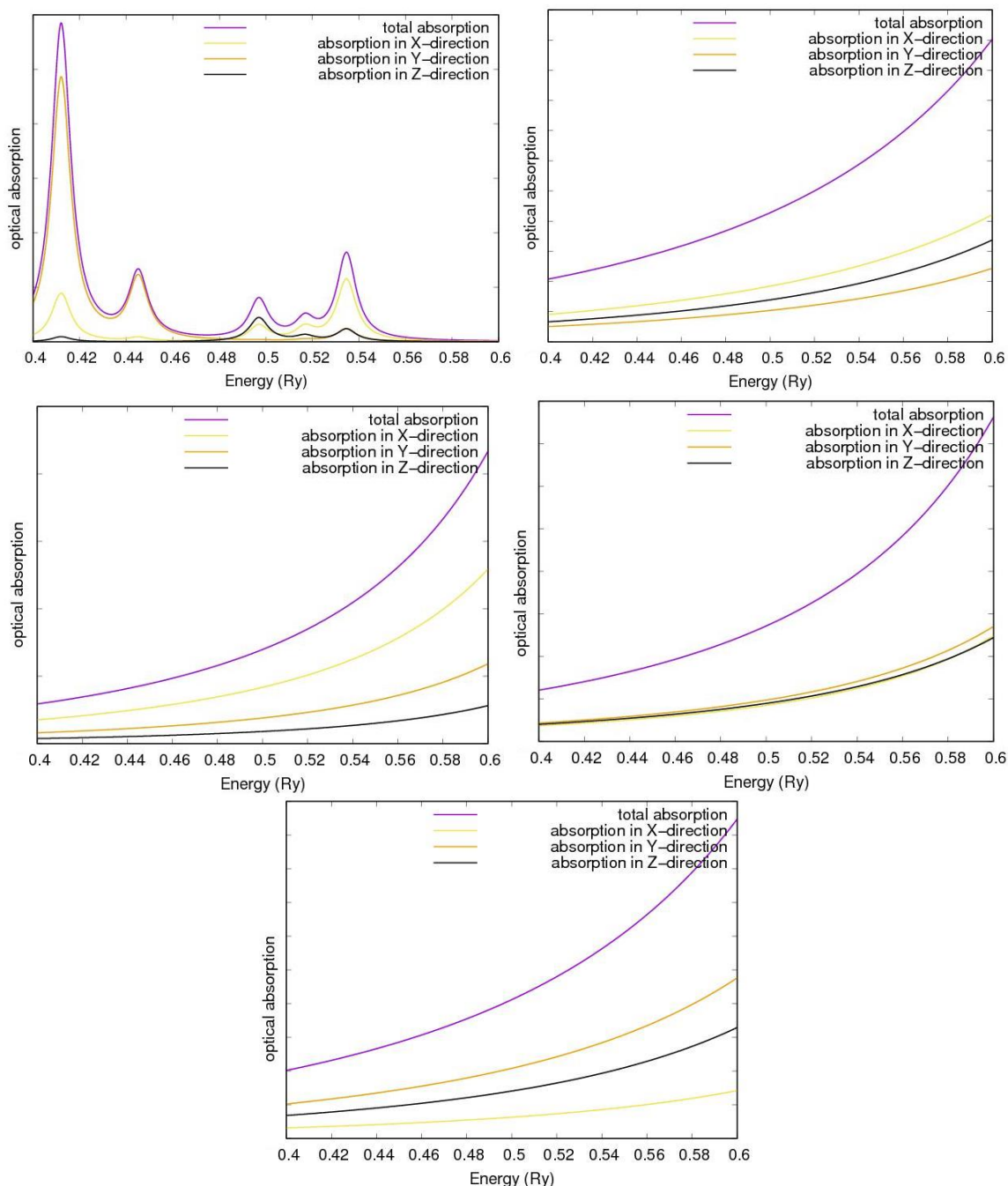


Figure 6. Optical absorption spectra for (a) PVK; (b) C₆₀; (c) PVK/C₆₀(1); (d) PVK/C₆₀(2); (e) PVK/C₆₀(3) configurations.

These observations are indications of processes of charge transfer taking place between C₆₀ and PVK. PVK ring deformation and stretching modes were affected by the C₆₀ inclusion into the network polymer. Direct interactions occur between C₆₀ and the main chain PVK through the transfer of charge processes.

3.6. Lowdin charge transfer.

In order to determine the transfer of charges from PVK to C₆₀, we projected the charge densities onto the atomic orbitals. Lowdin charge difference for pristine PVK and PVK/C₆₀ nano heterojunction was then noted as the charge transferred. We then determined the acceptor or donor characteristic of the adsorbate molecule. The charge transfer from the polymer, PVK, to the fullerene, C₆₀, in the configuration of PVK/C₆₀(3) turns out to be 0.19 electrons,

respectively, whereas for the configurations PVK/C60(1) and PVK/C60(2) we computed 0.11 and 0.12 electrons respectively in the opposite direction. Here, we would like to point out that the quantity of transferred charge obtained in the computation is controlled by the chosen approach to the calculation.

4. Conclusions

We adopted an *ab initio* approach, using the pseudopotential plane wave method to study the interaction of a conjugated polymer, PVK, with fullerene, C₆₀. A novel nanoheterostructure interface has been synthesized by DFT methods with low-bandgap characteristics. This novel PVK/C₆₀ nanoheterostructure composite has a finite band gap and good stability and, therefore, has promising applications for photovoltaic devices. We propose PVK/C₆₀ nanoheterostructure as a potential candidate for use in photovoltaics, optoelectronics, and nanoelectronics devices.

Funding

This research received no external funding.

Acknowledgments

The authors would like to acknowledge the financial support from the Ghana Government Book and Research Allowance for tertiary institutions. V. W. E. acknowledges financial support from the Ministry of Science and Technology for the grant of FICCI of New Delhi for fellowship. The authors are grateful to the Centre for High-Performance Computing (CHPC), Cape Town, South Africa, for computer time on the Lengau cluster.

Conflicts of Interest

The authors declare no conflict of interest.

References

1. Chapin, D.M.; Fuller, C.S.; Pearson, G.L. A new silicon p-n junction photocell for converting solar radiation into electrical power. *J. Appl. Phys.* **1954**, *25*, 676–677, <https://doi.org/10.1063/1.1721711>.
2. Hanjun, Z.; Huan, B.; Yongheng, C.; Mengna, G.; Wenjing, H.; Pengyu, S.; Kai, Z.; Yang, C.; Gong, X.; Xiao, L.; Liu, L. Functionalized polymer modified buried interface for enhanced efficiency and stability of perovskite solar cells. *Nanoscale* **2023**, *15*, 2054–2060, <https://doi.org/10.1039/D2NR06290A>.
3. Marks, R.N.; Halls, J. J. M.; Bradley, D.D.C.; Friend, R.H.; Holmes, A.B. The photovoltaic response in poly(p-phenylene vinylene) thin-film devices. *J. Phys. Condens. Matter.* **1994**, *6*, 1379–1394, <https://doi.org/10.1088/0953-8984/6/7/009>.
4. Tang, C.W. Two-layer organic photovoltaic cell. *Appl. Phys. Lett.* **1986**, *48*, 183–185, <https://doi.org/10.1063/1.96937>.
5. Knupfer, M. Exciton binding energies in organic semiconductors. *Appl. Phys. A* **2003**, *77*, 623–626, <https://doi.org/10.1007/s00339-003-2182-9>.
6. Yu, G.; Gao, J.; Hummelen, J.C.; Wudl, F.; Heeger, A.J. Polymer photovoltaic cells: Enhanced efficiencies via a network of internal donor-acceptor heterojunctions. *Science* **1995**, *270*, 1789, <https://doi.org/10.1126/science.270.5243.1789>.
7. Liu, Q.; Jiang, Y.; Jin, K.; Qin, J.; Xu, J.; Li, W.; Xiong, J.; Liu, J.; Xiao, Z.; Sun, K. 18% Efficiency organic solar cells. *Sci. Bull.* **2020**, *65*, 272–275, <https://doi.org/10.1016/j.scib.2020.01.001>.
8. Lin, Y.; Firdaus, Y.; Isikgor, F.H.; Nugraha, M.I.; Yengel, E.; Harrison, G.T.; Hallani, R.; El-Labban, A.; Faber, H.; Ma, C. Self-assembled monolayer enables hole transport layer-free organic solar cells with 18% efficiency and improved operational stability. *ACS Energy Lett.* **2020**, *5*, 2935–2944, <https://doi.org/10.1021/acsenerylett.0c01421>.

9. Lin, Y.; Nugraha, M.I.; Firdaus, Y.; Scaccabarozzi, A.D.; Aniés, F.; Emwas, A.-H.; Yengel, E.; Zheng, X.; Liu, J.; Wahyudi, W.; *et al.* A simple n-dopant derived from diquat boosts the efficiency of organic solar cells to 18.3%. *ACS Energy Lett.* **2020**, *5*, 3663–3671, <https://doi.org/10.1021/acsenerylett.0c01949>.
10. Fan, J. Y. High-performance organic solar modules via the bilayer-merged annealing assisted blading coating. *Adv. Mater.* **2022**, *34*, 2110569, <https://doi.org/10.1002/adma.202110569>.
11. Zhao, W.; Qian, D.; Zhang, S.; Li, S.; Inganäs, O.; Gao, F.; Hou, J. Fullerene-free polymer solar cells with over 11% efficiency and excellent thermal stability. *Adv. Mater.* **2016**, *28*, 4734–4739, <https://doi.org/10.1002/adma.201600281>.
12. Lin, Y.; Zhao, F.; He, Q.; Huo, L.; Wu, Y.; Parker, T.C.; Ma, W.; Sun, Y.; Wang, C.; Zhu, D. High-performance electron acceptor with thienyl side chains for organic photovoltaics. *J. Am. Chem. Soc.* **2016**, *138*, 4955–4961, <https://doi.org/10.1021/jacs.6b02004>.
13. Zhu, L.; Zhong, W.; Qiu, C.; Lyu, B.; Zhou, Z.; Zhang, M.; Song, J.; Xu, J.; Wang, J.; Ali, J. Aggregation-induced multilength scaled morphology enabling 11.76% efficiency in all-polymer solar cells using printing fabrication. *Adv. Mater.* **2019**, *31*, 1902899, <https://doi.org/10.1002/adma.201902899>.
14. Zhao, R.; Wang, N.; Yu, Y.; Liu, J. Organoboron polymer for 10% efficiency all-polymer solar cells. *Chem. Mater.* **2020**, *32*, 1308–1314, <https://doi.org/10.1021/acs.chemmater.9b04997>.
15. Chen, J.-D.; Cui, C.; Li, Y.-Q.; Zhou, L.; Ou, Q.-D.; Li, C.; Li, Y.; Tang, J. X. Single-junction polymer solar cells exceeding 10% power conversion efficiency. *Adv. Mater.* **2015**, *27*, 1035–1041, <https://doi.org/10.1002/adma.201404535>.
16. Zhao, J.; Li, Y.; Yang, G.; Jiang, K.; Lin, H.; Ade, H.; Ma, W.; Yan, H. Efficient organic solar cells processed from hydrocarbon solvents. *Nat. Energy* **2016**, *1*, 15027, <https://doi.org/10.1038/nenergy.2015.27>.
17. Zhang, S.; Qin, Y.; Zhu, J.; Hou, J. Over 14% efficiency in polymer solar cells enabled by a chlorinated polymer donor. *Adv. Mater.* **2018**, *30*, 1800868, <https://doi.org/10.1002/adma.201800868>.
18. Ma, R.; Liu, T.; Luo, Z.; Guo, Q.; Xiao, Y.; Chen, Y.; Li, X.; Luo, S.; Lu, X.; Zhang, M. Improving open-circuit voltage by a chlorinated polymer donor endows binary organic solar cells efficiencies over 17%. *Sci. China Chem.* **2020**, *63*, 325–330, <https://doi.org/10.1007/s11426-019-9669-3>.
19. Zheng, Z.; Wang, J.; Bi, P.; Ren, J.; Wang, Y.; Yang, Y.; Liu, X.; Zhang, S.; Hou, J. Tandem organic solar cell with 20.2% efficiency. *Joule* **2022**, *6*, 171–184, <https://doi.org/10.1016/j.joule.2021.12.017>.
20. Cui, Y.; Yao, H.F.; Xu, Y. 100 cm² Organic Photovoltaic Cells with 23% Efficiency under Indoor Illumination. *Chin J Polym Sci* **2022**, *40*, 979–988. <https://doi.org/10.1007/s10118-022-2761-x>.
21. Jin, K.; Xiao, Z.; Ding, L. 18.69% PCE from organic solar cells. *J. Semic.* **2021**, *42*, 060502, <https://doi.org/10.1088/1674-4926/42/6/060502>.
22. Peng, W. Over 18% ternary polymer solar cells enabled by a terpolymer as the third component. *Nano Energy* **2022**, *92*, 106681, <https://doi.org/10.1016/j.nanoen.2021.106681>.
23. Zhang, M. Single-layered organic photovoltaics with double cascading charge transport pathways: 18% efficiencies. *Nat. Comm.* **2021**, *12*, 309, <https://doi.org/10.1038/s41467-020-20580-8>.
24. Cui, Y. Single-Junction Organic Photovoltaic Cell with 19% Efficiency. *Adv. Mater.* **2021**, *33*, 2102420, <https://doi.org/10.1002/adma.202102420>.
25. Chong, K. Realizing 19.05% Efficiency Polymer Solar Cells by Progressively Improving Charge Extraction and Suppressing Charge Recombination. *Adv. Mater.* **2022**, *34*, 2109516, <https://doi.org/10.1002/adma.202109516>.
26. Li, G. Non-fullerene acceptors with direct and indirect hexa-fluorination afford >17% efficiency in polymer solar cells. *Energy Environ. Sci.* **2022**, *15*, 645–659, <https://doi.org/10.1039/D1EE03225A>.
27. Chen, H.; A guest-assisted molecular-organization approach for >17% efficiency organic solar cells using environmentally friendly solvents. *Nat. Energy* **2021**, *6*, 1045–1053, <https://doi.org/10.1038/s41560-021-00923-5>.
28. Kong, X.; 18.55% efficiency polymer solar cells based on a small molecule acceptor with alkylthienyl outer side chains and a low-cost polymer donor PTQ10. *CCS Chem.* **2022**, *22*, 2056, <https://doi.org/10.31635/ccschem.022.202202056>.
29. Xu, X.; Zhang, G.; Li, Y.; Peng, Q. The recent progress of wide bandgap donor polymers towards non-fullerene organic solar cells. *Chin. Chem. Lett.* **2019**, *30*, 809–825, <https://doi.org/10.1016/j.ccl.2019.02.030>.
30. Dey, S. Recent progress in molecular design of fused ring electron acceptors for organic solar cells. *Small* **2019**, *15*, 1900134, <https://doi.org/10.1002/sml.201900134>.
31. Dou, L.; Woongsik, J.; Dickson, D. B.; Min, S. K.; Dong, H. W.; Aung, K. K. K. Recent progress in organic solar cells based on non-fullerene acceptors: materials to devices. *J. Mater. Chem. A* **2022**, *10*, 3255, <https://pubs.rsc.org/en/content/articlelanding/2022/ta/d1ta10707k>.
32. Baobing, F.; Wei, G.; Xuanhao, W.; Xinxin, X.; Yue, W.; Francis, R. L.; Qunping, F.; Xinhui, L.; Wen, J. L.; Wei, M.; Alex, K. Y. J. Importance of structural hinderance in performance–stability equilibrium of organic photovoltaics. *Nature Comm.* **2022**, *13*, 5946, <https://doi.org/10.1038/s41467-022-33754-3>.
33. Liu, H. Technical challenges and perspectives for the commercialization of solution-processable solar cells. *Adv. Mater. Tech.* **2021**, *6*, 2000960, <https://doi.org/10.1002/admt.202000960>.

34. Zuo, L. Dilution effect for highly efficient multiple-component organic solar cells. *Nat. Nanotech.* **2022**, *17*, 53–60, <https://doi.org/10.1038/s41565-021-01011-1>.
35. Fan, B. Enabling high-performance, centimeter-scale organic solar cells through three-dimensional charge transport. *Cell Rep. Phys. Sci.* **2022**, *3*, 100761, <https://doi.org/10.1016/j.xcrp.2022.100761>.
36. Li, G.; Zhu, R.; Yang, Y. Polymer solar cells. *Nat. Photon.* **2012**, *6*, 153–161, <https://doi.org/10.1038/nphoton.2012.11>.
37. Günes, S.; Neugebauer, H.; Sariciftci, N. S. Conjugated polymer-based organic solar cells. *Chem. Rev.* **2007**, *107*, 1324–1338, <https://doi.org/10.1021/cr050149z>.
38. Sorrentino, R.; Kozma, E.; Luzzati, S.; Po, R. Interlayers for non-fullerene-based polymer solar cells: distinctive features and challenges. *Energy Environ. Sci.* **2021**, *14*, 180–223, <https://doi.org/10.1039/D0EE02503H>.
39. Cui, Y. Single-junction organic photovoltaic cells with approaching 18% efficiency. *Adv. Mater.* **2020**, *32*, 1908205, <https://doi.org/10.1002/adma.201908205>.
40. Zhan, L. Over 17% efficiency ternary organic solar cells enabled by two non-fullerene acceptors working in an alloy-like model. *Energy Environ. Sci.* **2020**, *13*, 635–645, <https://doi.org/10.1039/C9EE03710A>.
41. Zhan, L. Desired open-circuit voltage increase enables efficiencies approaching 19% in symmetric-asymmetric molecule ternary organic photovoltaics. *Joule* **2022**, *6*, 662–675, <https://doi.org/10.1016/j.joule.2022.02.001>.
42. Zhu, L. Single-junction organic solar cells with over 19% efficiency enabled by a refined double-fibril network morphology. *Nat. Mater.* **2022**, *21*, 656–663, <https://doi.org/10.1038/s41563-022-01244-y>.
43. Zhao, F. Single-junction binary-blend non-fullerene polymer solar cells with 12.1% efficiency. *Adv. Mater.* **2017**, *29*, 1700144, <https://doi.org/10.1002/adma.201700144>.
44. Zhao, W. Fullerene-free polymer solar cells with over 11% efficiency and excellent thermal stability. *Adv. Mater.* **2016**, *28*, 4734–4739, <https://doi.org/10.1002/adma.201600281>.
45. Mao, L. Writable and patternable organic solar cells and modules inspired by an old Chinese calligraphy tradition. *Mater. Horiz.* **2018**, *5*, 123–130, <https://doi.org/10.1039/C7MH00559H>.
46. Yuan, J. Single-junction organic solar cell with over 15% efficiency using fused-ring acceptor with electron-deficient core. *Joule* **2019**, *3*, 1140–1151, <https://doi.org/10.1016/j.joule.2019.01.004>.
47. Wang, W. Fused hexacyclic non-fullerene acceptor with strong near-infrared absorption for semitransparent organic solar cells with 9.77% efficiency. *Adv. Mater.* **2017**, *29*, 1701308, <https://doi.org/10.1002/adma.201701308>.
48. Dennler, G.; Scharber, M. C.; Brabec, C. J. Polymer-fullerene bulk-heterojunction solar cells. *Adv. Mater.* **2009**, *21*, 1323–1338, <https://doi.org/10.1002/adma.200801283>.
49. Li, S. Efficient organic solar cells with non-fullerene acceptors. *Small* **2017**, *13*, 1701120, <https://doi.org/10.1002/sml.201701120>.
50. Li, W.; Liu, D.; Wang, T. Stability of non-fullerene electron acceptors and their photovoltaic devices. *Adv. Funct. Mater.* **2021**, *31*, 2104552, <https://doi.org/10.1002/adfm.202104552>.
51. Che, Y.; Rizwan, N. M.; Izquierdo, R.; Perepichka, D. F. Mechanism of the photodegradation of A-D-A acceptors for organic photovoltaics. *Angew. Chem.* **2021**, *133*, 25037–25041, <https://doi.org/10.1002/anie.202109357>.
52. Hung, K. E. Non-volatile perfluorophenyl-based additive for enhanced efficiency and thermal stability of non-fullerene organic solar cells via supramolecular fluorinated interactions. *Adv. Energy Mater.* **2022**, *12*, 2103702, <https://doi.org/10.1002/aenm.202103702>.
53. Ghasemi, M. A molecular interaction-diffusion framework for predicting organic solar cell stability. *Nat. Mater.* **2021**, *20*, 525–532, <https://doi.org/10.1038/s41563-020-00872-6>.
54. Fan, B. Enabling High Efficiency of Hydrocarbon-Solvent Processed Organic Solar Cells through Balanced Charge Generation and Non-Radiative Loss. *Adv. Energy Mater.* **2021**, *11*, 2101768, <https://doi.org/10.1002/aenm.202101768>.
55. Cui, Y. Wide-gap non-fullerene acceptor enabling high-performance organic photovoltaic cells for indoor applications. *Nat. Energy* **2019**, *4*, 768–775, <https://doi.org/10.1038/s41560-019-0448-5>.
56. Wang, Y. Recent progress and challenges toward highly stable non-fullerene acceptor-based organic solar cells. *Adv. Energy Mater.* **2021**, *11*, 2003002, <https://doi.org/10.1002/aenm.202003002>.
57. Dai, S.; Zhan, X. Non-fullerene acceptors for semitransparent organic solar cells. *Adv. Energy Mater.* **2018**, *8*, 1800002, <https://doi.org/10.1002/aenm.201800002>.
58. Liu, B. Achieving highly efficient all-polymer solar cells by green-solvent-processing under ambient atmosphere. *Energy Environ. Sci.* **2021**, *14*, 4499–4507, <https://doi.org/10.1039/D1EE01310F>.
59. Qin, Y. The performance-stability conundrum of BTP-based organic solar cells. *Joule* **2021**, *5*, 2129–2147, <https://doi.org/10.1016/j.joule.2021.06.006>.
60. Zhang, X. High fill factor organic solar cells with increased dielectric constant and molecular packing density. *Joule* **2022**, *6*, 444–457, <https://doi.org/10.1016/j.joule.2022.01.006>.
61. Fan, B. Formation of vitrified solid solution enables simultaneously efficient and stable organic solar cells. *ACS Energy Lett.* **2021**, *6*, 3522–3529, <https://doi.org/10.1021/acsenenergylett.1c01576>.

62. Zhang, J. Alkyl-chain branching of non-fullerene acceptors flanking conjugated side groups toward highly efficient organic solar cells. *Adv. Energy Mater.* **2021**, *11*, 2102596, <https://doi.org/10.1002/aenm.202102596>.
63. Lipomi, D. J.; Tee, B. C.-K.; Vosgueritchian, M.; Bao, Z. Stretchable organic solar cells. *Adv. Mater.* **2011**, *23*, 1771–1775, <https://doi.org/10.1002/adma.201004426>.
64. Qin, F. Robust metal ion-chelated polymer interfacial layer for ultra-flexible non-fullerene organic solar cells. *Nat. Commun.* **2020**, *11*, 4508, <https://doi.org/10.1038/s41467-020-18373-0>.
65. Kaltenbrunner, M. Ultrathin and lightweight organic solar cells with high flexibility. *Nat. Commun.* **2012**, *3*, 770, <https://doi.org/10.1038/ncomms1772>.
66. Jinno, H. Stretchable and waterproof elastomer-coated organic photovoltaics for washable electronic textile applications. *Nat. Energy* **2017**, *2*, 780–785, <https://doi.org/10.1038/s41560-017-0001-3>.
67. Gaynor, W.; Lee, J. Y.; Peumans, P. Fully solution-processed inverted polymer solar cells with laminated nanowire electrodes. *ACS Nano* **2010**, *4*, 30–34, <https://doi.org/10.1021/nn900758e>.
68. Yim, J. H. Fully solution-processed semitransparent organic solar cells with a silver nanowire cathode and a conducting polymer anode. *ACS Nano* **2014**, *8*, 2857–2863, <https://doi.org/10.1021/nn406672n>.
69. Brabec, C. J.; Durrant, J. R. Solution-processed organic solar cells. *MRS Bull.* **2011**, *33*, 670–675, <https://doi.org/10.1557/mrs2008.138>.
70. Krebs, F. C.; Gevorgyan, S. A.; Alstrup, J. A roll-to-roll process to flexible polymer solar cells: model studies, manufacture and operational stability studies. *J. Mater. Chem.* **2009**, *19*, 5442–5451, <https://doi.org/10.1039/B823001C>.
71. Berny, S. Solar trees: first large-scale demonstration of fully solution coated, semitransparent, flexible organic photovoltaic modules. *Adv. Sci.* **2016**, *3*, 1500342, <https://doi.org/10.1002/advs.201500342>.
72. Gu, X. Roll-to-roll printed large-area all-polymer solar cells with 5% efficiency based on a low crystallinity conjugated polymer blend. *Adv. Energy Mater.* **2017**, *7*, 1602742, <https://doi.org/10.1002/aenm.201602742>.
73. Kong, X. The effect of alkyl substitution position of thienyl outer side chains on photovoltaic performance of A–DA'D–A type acceptors. *Energy Environ. Sci.* **2022**, *15*, 2011–2020, <https://doi.org/10.1039/D2EE00430E>.
74. Perdígón-Toro, L. Excitons dominate the emission from PM6:Y6 solar cells, but this does not help the open-circuit voltage of the device. *ACS Energy Lett.* **2021**, *6*, 557–564, <https://doi.org/10.1021/acsenenergylett.0c02572>.
75. Chen, X.-K. A unified description of non-radiative voltage losses in organic solar cells. *Nat. Energy* **2021**, *6*, 799–806, <https://doi.org/10.1038/s41560-021-00843-4>.
76. Liu, Q. Narrow electroluminescence linewidths for reduced nonradiative recombination in organic solar cells and near-infrared light-emitting diodes. *Joule* **2021**, *5*, 2365–2379, <https://doi.org/10.1016/j.joule.2021.06.010>.
77. Xia, X. Uncovering the out-of-plane nanomorphology of organic photovoltaic bulk heterojunction by GTSAXS. *Nat. Commun.* **2021**, *12*, 6226, <https://doi.org/10.1038/s41467-021-26510-6>.
78. Jung, S. All-inkjet-printed, all-air-processed solar cells. *Adv. Energy Mater.* **2014**, *4*, 1400432, <https://doi.org/10.1002/aenm.201400432>.
79. Angmo, D. Roll-to-roll printed silver nanowire semitransparent electrodes for fully ambient solution-processed tandem polymer solar cells. *Adv. Funct. Mater.* **2015**, *25*, 4539–4547, <https://doi.org/10.1002/adfm.201501887>.
80. Krebs, F. C. All solution roll-to-roll processed polymer solar cells free from indium-tin-oxide and vacuum coating steps. *Org. Electron.* **2009**, *10*, 761–768, <https://doi.org/10.1016/j.orgel.2009.03.009>.
81. Hong, S. Effect of solvent on large-area polymer-fullerene solar cells fabricated by a slot-die coating method. *Sol. Energy Mater. Sol. Cells* **2014**, *126*, 107–112, <https://doi.org/10.1016/j.solmat.2014.03.042>.
82. Carlé, J. E. Upscaling from single cells to modules-fabrication of vacuum-and ITO-free polymer solar cells on flexible substrates with long lifetime. *J. Mater. Chem.* **2014**, *C2*, 1290–1297, <https://doi.org/10.1039/C3TC31859A>.
83. Krebs, F. C.; Tromholt, T.; Jorgensen, M. Upscaling of polymer solar cell fabrication using full roll-to-roll processing. *Nanoscale* **2010**, *2*, 873–886, <https://doi.org/10.1039/B9NR00430K>.
84. Guo, F. Fully printed organic tandem solar cells using solution-processed silver nanowires and opaque silver as charge collecting electrodes. *Energy Environ. Sci.* **2015**, *8*, 1690–1697, <https://doi.org/10.1039/C5EE00184F>.
85. Fu, Y.; Huang, Y.; Li, Y.; Li, Y. Large-area flexible organic solar cells. *npj Flex. Electron.* **2021**, *5*, 30, <https://doi.org/10.1038/s41528-021-00128-6>.
86. Li, Y.; Xu, G.; Cui, C.; Li, Y. Flexible and semitransparent organic solar cells. *Adv. Energy Mater.* **2018**, *8*, 1701791, <https://doi.org/10.1002/aenm.201701791>.
87. Chen, X. Realizing ultrahigh mechanical flexibility and >15% efficiency of flexible organic solar cells via a "welding" flexible transparent electrode. *Adv. Mater.* **2020**, *32*, 1908478, <https://doi.org/10.1002/adma.201908478>.
88. Zeng, G. Breaking 12% efficiency in flexible organic solar cells by using a composite electrode. *Sci. China Chem.* **2019**, *62*, 851–858, <https://doi.org/10.1007/s11426-018-9430-8>.

89. Elloh, V. W. Poly(9-Vinylcarbazole)/Graphene Nanoheterostructure Interfaces: Ab Initio Dynamics Studies for Photovoltaic and Optoelectronic Applications. *Biointerface Research in Applied Chemistry* **2023**, *13*, 399. <https://doi.org/10.33263/BRIAC134.399>.
90. Sun, L. Flexible all-solution-processed organic solar cells with high-performance non-fullerene active layers. *Adv. Mater.* **2020**, *32*, 1907840, <https://doi.org/10.1002/adma.201907840>.
91. Scharber, M. C.; Sariciftci, N. S. Efficiency of bulk-heterojunction organic solar cells. *Prog. Polym. Sci.* **2013**, *38*, 1929–1940, <https://doi.org/10.1016/j.progpolymsci.2013.05.001>.
92. Giannozzi, P.; Andreussi, O.; Brumme, T.; Bunau, O.; Buongiorno, M. Advanced capabilities for materials modelling with Quantum ESPRESSO, *J. Phys. Conde. Matt.* **2017**, *29*, <https://doi.org/10.1088/1361-648X/aa8f79>
93. <http://www.quantum-espresso.org>.
94. Perdew, J. P.; Zunger, A.; *Phys. Rev. B* **1981**, *23*, 5048–5079, <https://doi.org/10.1103/PhysRevB.23.5048>
95. Rappe, A. M. K.; Rabe, M.; Kaxiras, E.; Joannopoulos, J. D. Optimized pseudopotentials, *Phys. Rev.* **1990**, *B 41*, 1227–1230, <https://doi.org/10.1103/PhysRevB.41.1227>.
96. Perdew, J. P.; Burke, K.; Ernzerhof, M. Generalized Gradient Approximation Made Simple. *Phys. Rev. Lett.* **1996**, *77*, 3865, <https://doi.org/10.1103/PhysRevLett.77.3865>.
97. Grimme, S.; Antony, J.; Ehrlich, S.; Krieg, H. A Consistent and Accurate Ab Initio Parametrization of Density Functional Dispersion Correction (DFT-D) for the 94 Elements H-Pu, *J. Chem. Phys.* **2010**, *132*, 154104, <https://doi.org/10.1063/1.3382344>.
98. Park, H.; Koh, H. S.; Siegel, D. J. First-Principles Study of Redox End Members in Lithium–Sulfur Batteries, *J. Phys. Chem.* **2015**, *C119*, 4675–4683, <https://doi.org/10.1021/jp513023v>.
99. Guo, Q.; Lau, K. C.; Pandey, R. A Xanes Study of Lithium Polysulfide Solids: A First-Principles Study, *Mater. Adv.* **2021**, *2*, 6403–6410, <https://doi.org/10.1039/D1MA00450F>.
100. Guo, Q.; Lau, K. C.; Pandey, R. Thermodynamic and Mechanical Stability of Crystalline Phases of Li₂S₂, *J. Phys. Chem.* **2019**, *C123*, 4674–4681, <https://doi.org/10.1021/acs.jpcc.8b11290>.
101. Sun, Q.; Lau, K. C.; Geng, D.; Meng, X. Atomic and Molecular Layer Deposition for Superior Lithium-Sulfur Batteries: Strategies, Performance and Mechanisms, *Batter. Super.* **2018**, *1*, 41–68, <https://doi.org/10.1557/s43578-020-00054-9>.
102. Momma, K.; Izumi, F. Vesta 3 for Three-Dimensional Visualization of Crystal, Volumetric and Morphology Data, *J. Appl. Crystal.* **2011**, *44*, 1272–1276, <https://doi.org/10.1107/S0021889811038970>.
103. Kokalj, A. Computer graphics and graphical user interfaces as tools in simulations of matter at the atomic scale, *Comp. Mater. Sci.* **2003**, *28*, 155-168, [https://doi.org/10.1016/S0927-0256\(03\)00104-6](https://doi.org/10.1016/S0927-0256(03)00104-6).
104. Hu, X. L.; Zhang, Y. F.; Zhuang, N. F.; Qian, J. Q. *Journal of Sol. Stat. Chem.* **2010**, *183*, 2741, <https://doi.org/10.1088/1742-6596/687/1/012048>.